Dynamic Forcing Behind Hurricane Lidia's Rapid Intensification

Mauricio López-Reyes[1,2,3], María Luisa Martín-Pérez[4,5], Carlos Calvo-Sancho[4,6], Juan Jesús González-Alemán[7]

[1]Instituto de Astronomía y Meteorología (IAM), Centro Universitario de Ciencias Exactas e Ingenierías (CUCEI), Departamento de Física, Universidad de Guadalajara, Guadalajara, Mexico.
[2]Department of Earth Physics and Astrophysics, Faculty of Physics, Complutense University of Madrid, Madrid, Spain.
[3]Instituto Frontera A.C., Departamento de Investigación, Tijuana, México.
[4]Department of Applied Mathematics, Faculty of Computer Engineering, University of Valladolid, Spain.
[5]Institute of Interdisciplinary Mathematics (IMI), Complutense University of Madrid, Madrid, Spain.
[6]Centro de Investigaciones sobre Desertificación, Consejo Superior de Investigaciones Científicas (CIDE, CSIC-UV-Generalitat Valenciana), Climate, Atmosphere and Ocean Laboratory (Climatoc-Lab), Moncada, Valencia, Spain
[7]Department of Development and Applications, Agencia Estatal de Meteorología (AEMET), Madrid, Spain.

Corresponding author: C. Calvo-Sancho (carlos.calvo.sancho@uva.es)

Key words

Rapid intensification, ensemble prediction, tropical cyclone, extratropical interactions

Key points

- A mid-to-upper level trough enhanced vertical motion and divergence over Hurricane Lidia, triggering rapid intensification.
- Stronger Trenberth forcing, eddy flux convergence, and vorticity advection were observed in ensemble members that captured RI.
- Ensemble diagnostics revealed that dynamic forcing preceded RI onset, suggesting a causal role beyond thermodynamic conditions.

Abstract

This study examines Hurricane Lidia's rapid intensification (RI) in the understudied northeastern Pacific, focusing on its interaction with an upper-level trough. Using IFS-ECMWF ensemble forecasts and ERA5 reanalysis, we analyze the large-scale dynamical mechanisms driving Lidia's intensification. Results show that the trough played a crucial role in promoting RI by enhancing synoptic-scale ascent, upper-level divergence, and eddy flux

44   convergence. In the higher-intensification ensemble group, stronger Trenberth forcing
45   emerged prior to RI onset, suggesting a causative role in preconditioning the storm
46   environment. This dynamical forcing likely triggered latent heat release, which in turn
47   modified the upper-level potential vorticity structure and contributed to a subsequent
48   reduction in vertical wind shear. In contrast, the lower-intensification group exhibited
49   weaker forcing, higher shear, and a lack of sustained ventilation. These findings highlight the
50   importance of diagnosing early dynamical triggers for RI, particularly in regions where
51   operational access to high-resolution models is limited. This approach provides a cost-
52   effective framework for anticipating RI using ensemble-based diagnostics and could serve
53   as a valuable forecasting tool in data-sparse areas such as the Pacific coast of Mexico. Future
54   studies should combine this large-scale methodology with high-resolution simulations to
55   better capture storm-scale processes and validate multi-scale interactions in RI events.
56
57
58
59
60
61
62
63
64
65
66
67
68
69
70
71
72
73
74
75
76
77
78
79
80
81
82
83
84
85
86
87

1 Introduction

México is among the countries most affected by tropical cyclones (TCs) from both the Atlantic and Pacific Oceans (Larson et al., 2005; López-Reyes et al., 2024). While the Atlantic basin has traditionally garnered more research attention, largely due to the severe economic and social impacts of TCs in the United States, there is a pressing need to expand research efforts in the northeastern Pacific basin, where fewer studies have been conducted (García Franco et al., 2024). In recent years, various major hurricanes, such as Patricia, Lidia, and Otis caused large economic losses and scores of deaths in México (Pasch, 2024; García Franco et al., 2024). These events also posed challenges for numerical weather prediction models, particularly in forecasting their tracks and intensification processes. As highlighted by Shi and Chen (2021), one of the key obstacles is improving the prediction of TCs that undergo rapid intensification (RI), defined as an increase of at least 30 kt ($\approx$ 54 km/h) in maximum sustained wind speed within a 24-h period (Kaplan and DeMaria, 2003). Recent studies have shown a rise in the frequency of RI events in the Atlantic basin, driven primarily by ocean warming (Majumdar et al., 2023; Li et al., 2023). The northeastern Pacific, however, has also experienced extreme intensification rates, with Patricia (2015), Willa (2018), and Otis (2023) ranking among the most rapidly intensifying storms on record. Similarly, during the 2024 hurricane season, Hurricane Milton underwent explosive intensification, posing a significant challenge for intensity forecasting (Pasch, 2024). Enhancing our ability to forecast RI is essential for reducing the risk these powerful storms pose to vulnerable communities and critical infrastructure.

Although RI is strongly influenced by thermodynamic factors, such as high sea surface temperatures (SSTs) and ocean heat content, dynamic factors also play a pivotal role. Interactions between TCs and upper-level troughs have been shown to significantly affect storm intensity (Fischer et al., 2019). According to Avila (1998), Hanley et al. (2001), López-Reyes et al. (2021) and DeMaria et al. (2021), forecasting intensity changes in TCs remains one of the biggest challenges, particularly during RI. The difficulties in forecasting RI stem from the complex factors involved in the occurrence of RI, such as the large-scale environment, internal dynamics and multiscale interactions (Kaplan et al., 2010; Zhang and Chen 2012; Bhalachandran at al., 2020; Wang et al., 2021; Shi and Chen 2021). Over the past few years, there has been notable progress in understanding the internal dynamics that govern RI. As found in Chen et al. (2019) and Shi and Chen (2021), the main dynamical and thermodynamic drivers of TC RI include strong upper-level divergence and strong boundary-layer convergence as well as a weak deep-layer vertical wind shear (VWS), higher relative humidity throughout the vertical column, and high intensification potential (details in Emanuel, 1988) associated with SST. Other studies have highlighted the significance of the deep convective region surrounding the eyewall and the large convergence of angular momentum into TC (Stevenson et al., 2014; Komaromi and Doyle 2018; Ryglicki et al., 2021). Furthermore, research studies have identified a relevant relationship between the structure and size of TCs, their environmental conditions, and the RI rate (Carrasco et al., 2014; Shi and Chen 2019; Tao et al., 2022; Ston et al., 2023; Nayaranan et al., 2024).

132 Since the general conditions favoring TC RI are well-known, other factors may influence
133 the overall intensification procesess. In a follow-up theoretical study, Lenoux et al. (2016)
134 identified an optimal TC-trough alignment that promotes interaction (Komaromi and Doyle
135 2018; Shato et al., 2020). Similarly, studies by DeMaria et al. (1993), Hanley et al. (2001),
136 and Peirano et al. (2016) suggest that an approaching upper-tropospheric trough can play a
137 critical role in hurricane intensification. However, trough interactions can also limit TC
138 intensification, depending on the configuration of the trough and its associated jet stream.
139 For example, increased dry air entrainment or increased VWS can inhibit TC development
140 (Peirano et al., 2016). Recent research has identified specific synoptic configurations that
141 favor RI, including short zonal wavelengths and favorable upstream displacements between
142 the TC and the trough (Fischer et al., 2019). Qiu et al. (2020) also showed how important
143 eddy flux convergence (EFC) is for making TC-trough interactions, particularly when large-
144 scale circulation patterns favor stronger upper-level divergence. In the same way, Yan et al.
145 (2021) found that upper-tropospheric cold lows could enhance EFC, reduce inertial stability,
146 and strengthen upper-level divergence, leading to RI. These studies show that TC-trough
147 interactions can have two effects and stress how important is to figure out what
148 environmental conditions make TC stronger or weaker.
149
150 Although TC–trough interactions have been extensively studied in the Atlantic basin, the
151 northeastern Pacific remains understudied. During El Niño events, the subtropical Pacific
152 warms considerably, increasing the likelihood of interactions between TCs and the jet
153 stream, increasing the likelihood of dynamic interactions (Luna-Niño et al., 2021; Ling et al.,
154 2024). In the Atlantic basin, on the other hand, these interactions often occur at higher
155 latitudes over less populated areas in the Atlantic basin. In contrast, TCs in the northeastern
156 Pacific tend to curve toward land, which puts densely populated areas in Mexico at risk. The
157 fact that warm SSTs and the jet stream interact during El Niño events shows how important
158 it is to do focused research in this area.
159
160 Additionally, the proximity of northeastern Pacific TCs to mountainous terrain introduces
161 further challenges for forecasting (DiMego et al., 1976). The most intense hurricanes that
162 have affected Mexico typically occur during late summer and early autumn, as was the case
163 with Hurricane Lidia in mid-October 2023. The devastating case of Hurricane Otis in October
164 2023, in which all global models failed to capture its RI, underscored the urgent need for
165 improved understanding of RI processes in this region. This event caused dozens of fatalities
166 and severe and widespread damages in Acapulco, highlighting Mexico's vulnerability to such
167 phenomena and the critical need for better forecast capabilities (Emanuel, 2024; Servicio
168 Meteorológico Nacional, 2023). Given the high SSTs during this season, trough-TC
169 interaction is particularly relevant during October and November, as many TCs turn
170 eastward during this period. This turning is influenced by the subtropical jet stream,
171 typically positioned between 25°N and 35°N, especially during seasons when El Niño events
172 are present (Luna-Niño et al., 2021; Tong et al., 2023). The jet stream may enhance
173 interactions between midlatitude troughs TCs; however, to the authors' knowledge, no
174 previous studies have specifically investigated the role of the jet stream in TC RI in the
175 northeastern Pacific. In contrast to most prior studies, which primarily focus on

176 thermodynamic drivers in the North Atlantic basin, our research emphasizes the dynamic
177 forcing mechanisms associated with trough-TC interactions, such as quasi-geostrophic
178 ascent, EFC, and enhanced upper-level divergence in the intensification of Hurricane Lidia.
179 By analyzing ensemble prediction system (EPS) outputs and ERA5 reanalysis data, we
180 provide a comprehensive assessment of the conditions that favored Lidia's RI, offering novel
181 insights into the dynamics of TC intensification in the northeastern Pacific.

183 Moreover, the northeastern Pacific lacks operational mesoscale models, making reliable
184 predictions of RI particularly challenging. In this context, EPSs have emerged as a valuable
185 tool for operational forecasting, providing insights into uncertainty and enabling the
186 evaluation of potential risk scenarios several days in advance. Using EPS outputs, this
187 study seeks to address these challenges and improve our understanding of the conditions
188 that favor RI in the northeastern Pacific.

190 This paper is organized as follows: Section 2 presents the data models and methods,
191 including the ensemble configurations and diagnostics tools. Section 3 describes the
192 synoptic conditions that influenced Hurricane Lidia's RI and the main dynamical processes
193 involved. Finally, Section 4 provides a summary of findings and concluding remarks.

195 **2   Data Models and Methods**

197 The data sets are based on forecasts from the Integrated Forecasting System (IFS) of the
198 European Centre for Medium-Range Weather Forecasts (ECMWF). This study uses the
199 operational perturbed forecast ensemble generated by the EPS (Cycle 48r1: ECMWF, 2023)
200 with 50 perturbed members is used. Each perturbed member has a horizontal resolution of
201 0.1° and 137 vertical levels. The last initialization is selected since it features a large spread
202 of Hurricane Lidia trajectories, corresponding to the October 8th, 00:00 UTC initialization,
203 with 1-hour time steps during 96 h. Additionally, to assess the performance of each
204 composite group, key atmospheric fields are computed using data from the ERA5 climate
205 reanalysis (Hersbach et al., 2020) with 0.25° horizontal resolution and 37 vertical levels,
206 during the period with the highest intensification rate.

208 Several dynamic and thermodynamic variables were utilized in this study, such as mean
209 sea level pressure ($MSLP$), temperature (T), geopotential height (Z), zonal and meridional
210 wind components (u, v), potential temperature (θ), SST and relative humidity (RH). See
211 Table 1 for additional details. To evaluate the role of the trough in the trajectory and
212 intensity change of Hurricane Lidia. Trajectories and intensification rate for all members are
213 determined using MSLP and divided them into two intensification rate groups (IRG) based
214 on the P_{20} (lower intensification rate) and P_{80} (highest intensification rate) percentiles of
215 MSLP. In addition, members who meet the RI definition are identified using wind threshold
216 criteria (greater than 54 km/h in 24-h). The NHC best track and official intensity data were
217 used for comparison with both groups. As is common in studies of this nature (Chen et al.,
218 2019; Chen et al., 2021; Hu and Zou, 2021; Collins et al., 2022), synoptic and storm-centered
219 composites (SCC) are derived for the specified fields within a circular area with an 8° radius.

220 **Table 1.** Details on the atmospheric variables used.

Variable	Symbol	Pressure levels (PVU)	Units
Mean sea level pressure	$MSLP$	Surface	hPa
Temperature	T	Surface, 1000, 925, 850, 700, 500, 400, 300, 250, 200	K
Geopotential height	Z	1000, 925, 850, 700, 500, 400, 300, 250, 200	m
Zonal wind component	u	850, 300, 200	ms^{-1}
Meridional wind component	v	850, 300, 200	ms^{-1}
Potential temperature	θ	(1.5-PVU)	K
Sea surface temperature	SST	Surface	K
Relative humidity	RH	500 hPa	%

221

222 Based on the previous variables, some derived fields related with TC intensity change
223 (Chen et al., 2021; Mei and Yu 2016) are also computed: VWS calculated between 850 and
224 200 hPa, irrotational wind ($\vec{V}_{irr}$) at 200 hPa, based on Helmholtz decomposition (details in
225 Chorin et al., 1990 and Cao et al., 2014) and vorticity advection, $\vec{V} \cdot \nabla(\vec{\xi} + f)$ at 500 hPa,
226 were $\vec{\xi} = \frac{\partial v}{\partial x} - \frac{\partial u}{\partial y}$ and f is the planetary vorticity.

227

228 Following Bister and Emanuel (1998) and Gilford (2021), potential intensity (PI) is also
229 calculated as

230

231 $PI = V_{max} = \left[\frac{C_k}{C_D} \frac{(T_s - T_0)}{T_0} (h_s^* - h^*) \right]^{1/2}$,

232

233 where C_k is the enthalpy surface exchange coefficient, C_D is the momentum surface
234 exchange coefficient, h_s^* is the saturation moist static energy at the sea surface, h^* is the
235 saturation moist static energy of the air above the boundary layer, following to Wing et al.
236 (2015), evaluated at 500-600 hPa. As mentioned in Gilford (2021), tropical cyclone
237 thermodynamic disequilibrium and efficiency were represented by terms $(h_0^* - h^*)$ and
238 $\frac{T_s - T_0}{T_0}$, where T_s is the sea surface temperature and T_0 is the outflow temperature level.

239

240 To identify regions that favor ascending air movements driven by synoptic-scale
241 dynamical forcing associated with extratropical systems (Loughe et al., 1995; Hanley et al.,
242 2001), ageostrophic wind ($\vec{V}_{ag}$) and its divergence ($\nabla \cdot \vec{V}_{ag}$) are additionally computed. The
243 quasi-geostrophic (QG) omega equation is also used to identify the synoptic ascent flow via
244 Trenberth form (Billingsley, 1998; Bracken and Bosart, 2000). Trenberth QG forcing (Q) is
245 calculated using the following expression

246

247 $Q = \left(\sigma \nabla_p^2 + f_0^2 \frac{\partial^2}{\partial p^2} \right) \omega \approx 2 \left[f_0 \frac{\partial \vec{V}_g}{\partial p} \cdot \nabla \left(\frac{\partial v}{\partial x} - \frac{\partial u}{\partial y} + f \right) \right]$,   (1)

248

249   i.e., vertical air movements are proportional to advection by vorticity by thermal wind.
250   Herein, σ is the stability parameter, f_0 the Coriolis parameter, ω the vertical component of
251   wind ($Pa \cdot s^{-1}$), $\vec{V}_g$ the geostrophic wind vector ($m\ s^{-1}$), p the pressure (Pa). Finally, with
252   the aim of measuring the degree of interaction between the trough and the TC, and
253   following previous studies in the Atlantic Ocean (Molinari and Vollaro, 1990; Hanley et al.,
254   2000; Komaromi and Doyle, 2018), the eddy flux convergence (EFC) is defined as
255
256   $$EFC = -\frac{1}{r^2}\frac{\partial}{\partial r}\left(r^2\overline{v_r'v_t'}\right), \qquad\qquad\qquad (2)$$
257
258   where v_r' is the perturbation radial wind, v_t' the perturbation tangential wind, and the
259   overbar denotes the azimuthal mean, computed in storm-relative coordinates. Based on the
260   methodology of DeMaria et al. (1993) and Hanley et al. (2001), the EFC is computed over a
261   radial range of 300 to 600 km for each time step during RI period.
262
263   To compare atmospheric fields between the most and least intensifying groups,
264   averages and standard deviations (STD) are calculated, and ensemble difference spatial
265   distributions ($P_{80} - P_{20}$) are generated to visualize the contrasts between the two groups.
266   In addition, time series of means and STDs of the thermodynamic and dynamic variables
267   analyzed between the groups during the simulation period are performed. Finally, a Mann-
268   Whitney U test is performed to identify regions with statistically significant differences at
269   the 95% confidence level (Mann and Whitney, 1947).
270
271   **3   Results**
272
273   3.1 Trajectory and intensity forecast analysis.
274
274   Hurricane Lidia originated from a tropical wave on 3 October 2023 (Pasch, 2024).
275   Between 3 and 5 October, it remained a disorganized system, marked by significant
276   uncertainty in both track and intensity forecasts (Figures S1). From 5 to 7 October, Lidia
277   generally tracked westward under the influence of a mid-level ridge but remained poorly
278   organized. By 8 October, the subtropical jet stream was positioned between 20° and 30°N,
279   aligned with Lidia's latitude. At this stage, a mid-to-upper-level trough approaching the Baja
280   California Peninsula began to influence Lidia's motion, steering the system northward and
281   subsequently eastward.
282
282   At approximately 18:00 UTC on 9 October, Lidia entered a phase of intensification
283   (Pasch, 2024). This intensification was accompanied by a northeastward turn induced by an
284   approaching trough from the northwest, although considerable spread in forecast
285   trajectories persisted at this time (Fig. 1a). On 10 October, Lidia underwent RI, with
286   maximum sustained winds increasing by 82 $km\ h^{-1}$ over an 18-hour period, ultimately
287   reaching a peak intensity of nearly 220 $km\ h^{-1}$. This placed Lidia at Category 4 on the Saffir–
288   Simpson Hurricane Wind Scale.
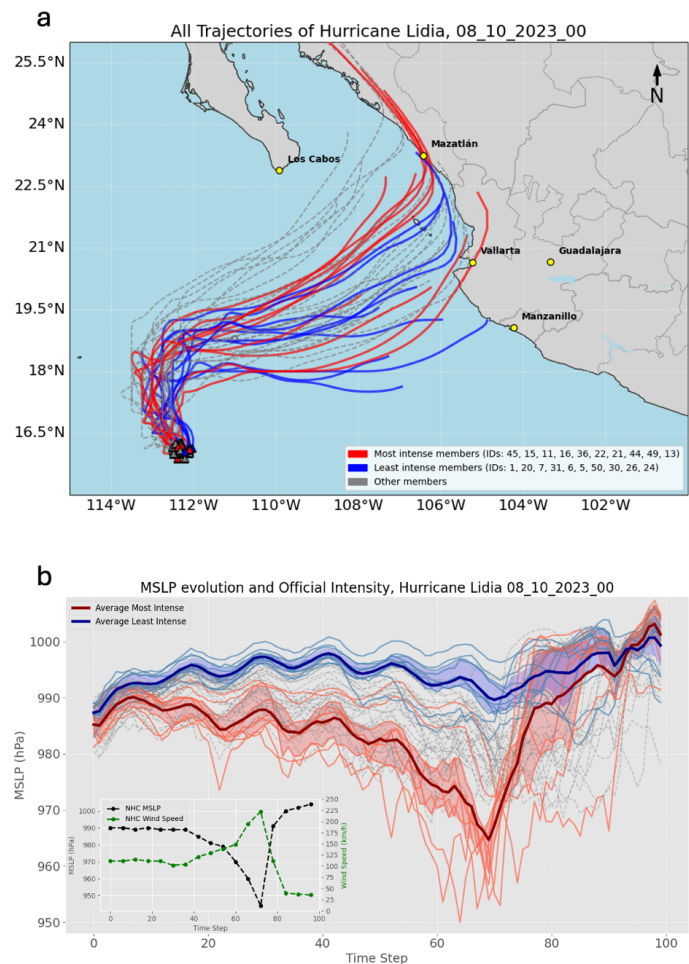
289
290 Figure 1. (a) Lidia's Trajectories for all members, highest (lower) IRG in red (blue) line and
291 best track of NHC (black line). (b) Intensity temporal evolution for all members (MSLP),
292 highest (lower) IRG in red (blue) line, shaded areas correspond with interquartile range; real
293 wind speed in green dotted line and MSLP in black dotted line.

294

295 Figure 1a shows the trajectories of Hurricane Lidia's ensemble members from the
296 ECMWF, initialized at 00:00 UTC on 8 October. The trajectories of the most intense members
297 are positioned further north relative to those of the lower-intensity members, relative to
298 the NHC best track. This demonstrates that the trough's proximity influenced event
299 predictability, increasing uncertainty in both track and intensity forecasts. This pattern
300 aligns with findings from Ito and Wu (2013), Callaghan (2020), and Sato et al. (2020) in the
301 Atlantic basin, indicating the contribution of synoptic environment to the low predictability
302 of both trajectory and intensity of the cyclone, as here evidenced by the large spread in
303 Figures 1a, b. Furthermore, based on Lidia's MSLP and wind speed temporal evolution (Fig.
304 1b), we observe that seven members corresponding to the P_{80}-ensemble, along with its

305   mean, successfully simulates Lidia's RI (Figure 1b). Although the simulated intensification is
306   slightly weaker, the timing is consistent with the actual RI period.
307
308   As is well known and formulated in the Emanuel model (Emanuel, 2002) and used in
309   Chen et al. (2021), the oceanic and atmospheric variables such as T_s, T_0 and saturation
310   parameters (eq. 1), determine the PI that the TC could acquire. Both ensembles display
311   similar PI distributions around Hurricane Lidia (Figs. 2a, b). However, somewhat
312   unexpectedly the P_{20}-ensemble shows a higher PI value ($\approx 250\ km\ h^{-1}$) compared to the
313   P_{80}-ensemble ($\approx 240\ km\ h^{-1}$), although the differences are not statistically significant (not
314   shown).
315
316   Based on the PI time series (Fig. 2c), this diagnostic variable alone does not appear to
317   support Lidia's RI. Therefore, this suggests that thermodynamic factors are necessary but
318   not sufficient to trigger RI. This finding is consistent with recent studies (e.g., Gilford, 2021;
319   Shi and Chen, 2021) which suggest that while PI provides an upper bound, the actual
320   intensification process is modulated by environmental dynamics, including ventilation and
321   vertical motion induced by synoptic-scale features such as upper-level troughs. These results
322   support the idea that synoptic-scale forcing may act as a precursor and driver of RI events.

323   Similarity, the spatial SST differences between the P_{80} and P_{20} ensembles (Fig. 3a–f)
324   reinforce the conclusion that thermodynamic conditions alone do not explain the
325   contrasting intensification outcomes. While some localized differences exceeding $\pm 5°C$
326   appear at specific time steps, these do not persist or align consistently with the RI period.
327   The warm anomalies observed in the P_{20} ensemble are mainly displaced to the north and
328   northeast of Lidia's core. This spatial misalignment suggests that, despite slightly warmer
329   SSTs, the coupling between oceanic energy supply and inner-core dynamics was likely
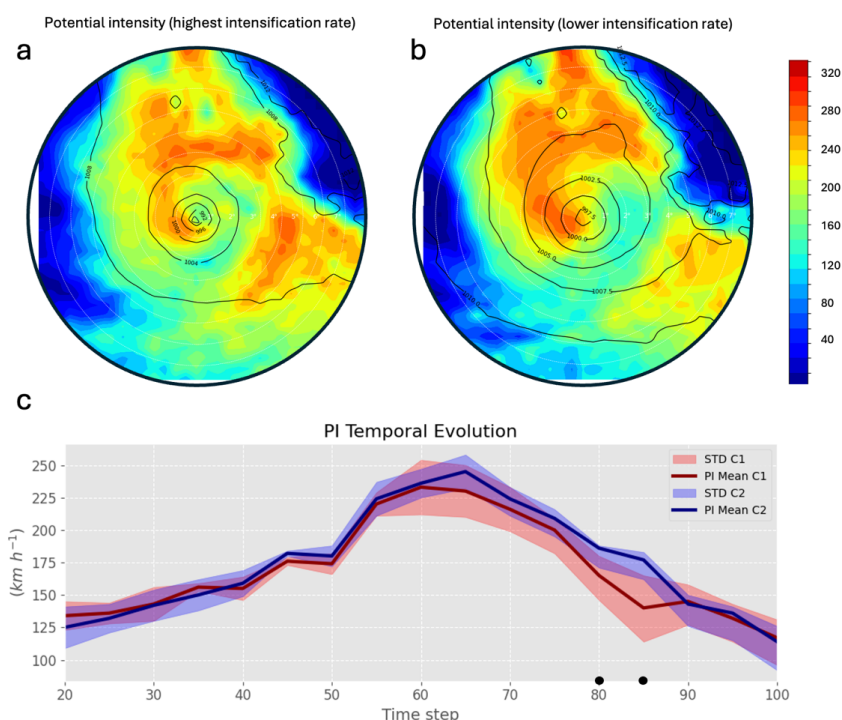330   suboptimal.

Figure 2. (a) Highest intensification rate PI SCC and (b) lower intensification rate PI SCC ($km\,h^{-1}$) at +55-h and (c) PI calculated within a radial range of with the red (blue) line representing the higher (lower) IRG. The red (blue) shaded regions indicate the STD for the highest (lower) IRG.

Statistical significance markers confirm that most SST anomalies are not spatially coherent enough to produce systematic differences in PI. This is consistent with the similar PI fields seen in both ensembles (Figs. 2a, b) and the absence of a clear thermodynamic advantage during the intensification period. Therefore, these SST patterns likely played a secondary role compared to the dynamically driven processes, such as enhanced vorticity advection and upper-level divergence.

This supports the notion that SSTs, in this case, provided a necessary but not sufficient condition for RI. The findings from Bister and Emanuel (2002) and Fischer et al. (2019) reinforces this view by emphasizing that, without favorable upper-level forcing and adequate storm structure, warm SSTs alone are insufficient to trigger RI, even when PI values appear theoretically consistent.
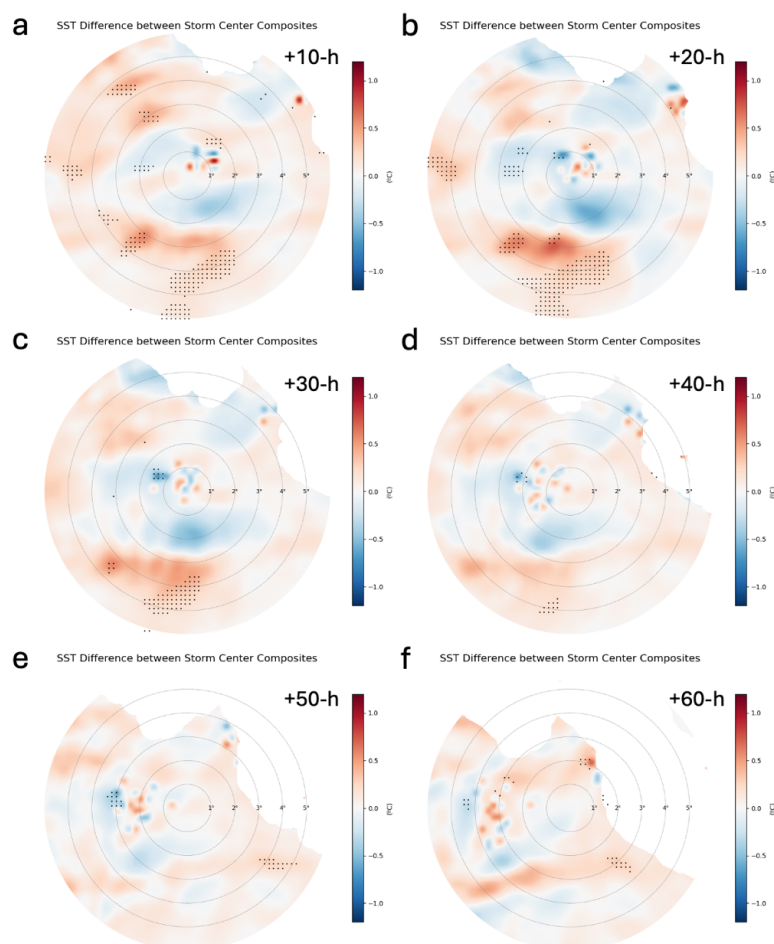
349 Figure 3. (a-f) SST difference maps (P_{80}-P_{20} ensembles; °C) for selected time steps from +10
350 h to +60 h. Dots indicate regions where differences are statistically significant at the 95%
351 confidence level.
352
353   3.2 Trough interaction and TC rapid intensification
354
355   Since thermodynamic factors fail to explain the differences observed among the
356 ensemble members in Lidia's intensification, we examine the mid- and upper-level dynamic
357 environment. Figure 4 shows the eastward progression of a trough in both ensemble groups.
358 The trough is notably broader in the P_{80}-ensemble, particularly from time step +55-h. At
359 250 and 300 hPa (Figs. 4a, b) the isohypses in the P_{80}-ensemble exhibit substantial
360 deformation toward Lidia. The trough deepens further in the P_{80} group at 500 hPa (Fig. 4c),
361 extending southward to approximately 20°N. This deep mid-tropospheric penetration is
362 critical because it aligns the trough with the steering and ventilation layers of the tropical
363 cyclone. The proximity of the trough to Lidia at this level likely contributed to a moist and

364   unstable environment ahead of the cyclone, while simultaneously promoting vorticity
365   advection and synoptic-scale positive vertical motions. This configuration aligns with
366   previous findings on optimal trough-tropical cyclone interactions (e.g., Hanley et al., 2001;
367   Fischer et al., 2019), which indicate that intensification is favored when the trough
368   approaches from the northwest at an appropriate distance.
369
370   The EFC is computed to diagnose the trough-TC interaction in Hurricane Lidia. The
371   results show significantly higher EFC values in P_{80}- than P_{20}-ensemble group. These
372   significant results are mainly localized between +50 h and +80 h from Lidia RI period (Fig. 5).
373   P_{80}-ensemble is closely aligns with ERA5 reanalysis (exceeding $10\ m\ s^{-1} day^{-1}$ during RI
374   period). These elevated EFC values are consistent with the findings of DeMaria et al. (1993)
375   for the North Atlantic basin, where EFC values greater than $10\ m\ s^{-1} day^{-1}$ serve as an
376   indicator of a trough-TC interaction. Therefore, the obtained EFC values highlight a strong
377   interaction between Lidia and the trough, suggesting that dynamic forcing, via quasi-
378   geostrophic approach, enhances vertical motion and upper-level ventilation, potentially
379   triggering RI. This behavior in the Pacific is analogous to the quasi-stationary effect of the
380   tropical upper tropospheric trough (TUTT) in the Caribbean, previously analyzed by Sanders
381   (1975). However, unlike the Caribbean TUTT, which tends to be more persistent and
382   conducive to cyclogenesis, the trough interacting with Hurricane Lidia in the Pacific is
383   transient and engages with an already mature TC. This suggests that it plays a crucial role in
384   Lidia's RI and its subsequent landward turn. Such interactions significantly increase the
385   potential risk for densely populated areas in Mexico, particularly during the late summer
386   months, when TCs are most frequent in the eastern Pacific basin (López-Reyes and
387   Meulenert, 2021).
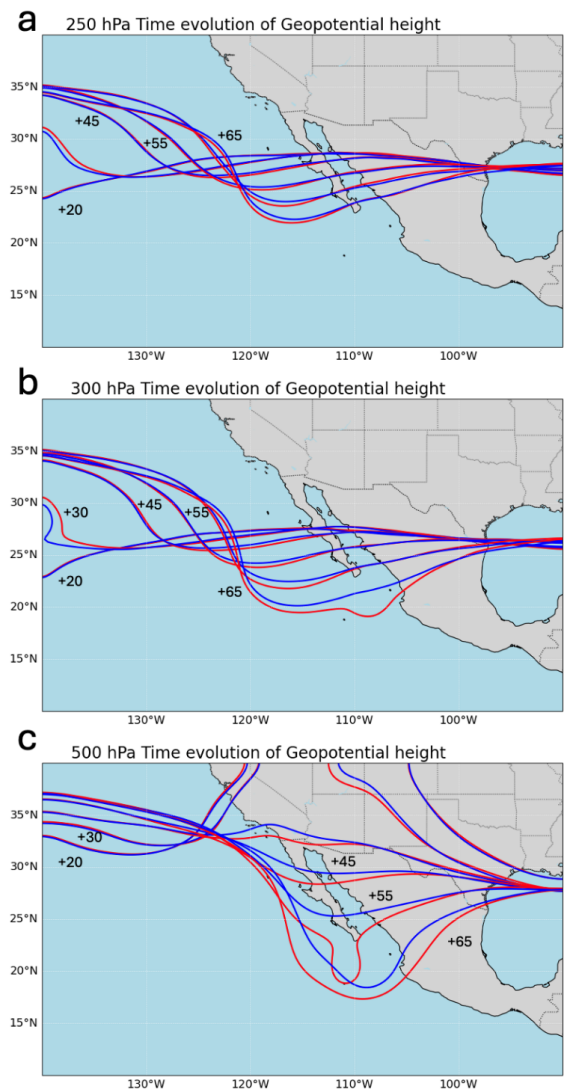
Figure 4. *Z* Composite corresponding to the highest (red contours) and lower (blue contours) IRG, at (a) 250 hPa, (b) 300 hPa and (c) 500 hPa, before and during the trough-TC interaction.

To assess the dynamical processes supporting Lidia's intensification, EPS outputs during the RI period are compared with ERA5 fields. Although typically applied in extratropical contexts, this approach is particularly relevant in the northeastern Pacific, where the subtropical jet can interact with TCs during autumn, and high-resolution forecast remains limited.
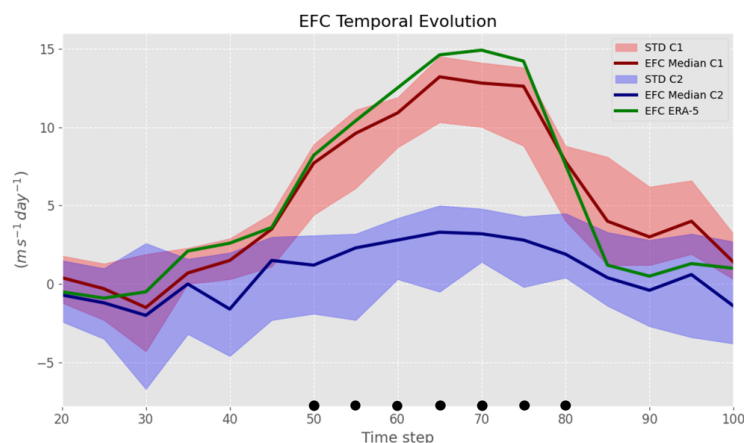
Figure 5. EFC temporal evolution calculated within a radial range of 300 to 600 km at 250 hPa, with the red (blue) line representing the higher (lower) IRG. The red (blue) shaded regions indicate the STD for the highest (lower) IRG, green line represents the EFC based on ERA5 data and dots indicate statistical significance.

In Figures 6a and 6b, the $\nabla \cdot \vec{V}_{ag} > 0$ values, associated with the trough and jet streak, are located to the northeast of Lidia. This configuration strongly favors enhanced upper-level divergence over Lidia and acts as a mechanism that drives upward motions. The quasi-geostrophic $\nabla \cdot \vec{V}_{ag}$ is notably higher in P_{80} than in P_{20}-ensemble (Fig. 6a-c); P_{80} closely matches ERA5 across nearly all regions surrounding Lidia (Fig. 6d), suggesting a stronger forcing induced by the interaction with the trough and jet streak.
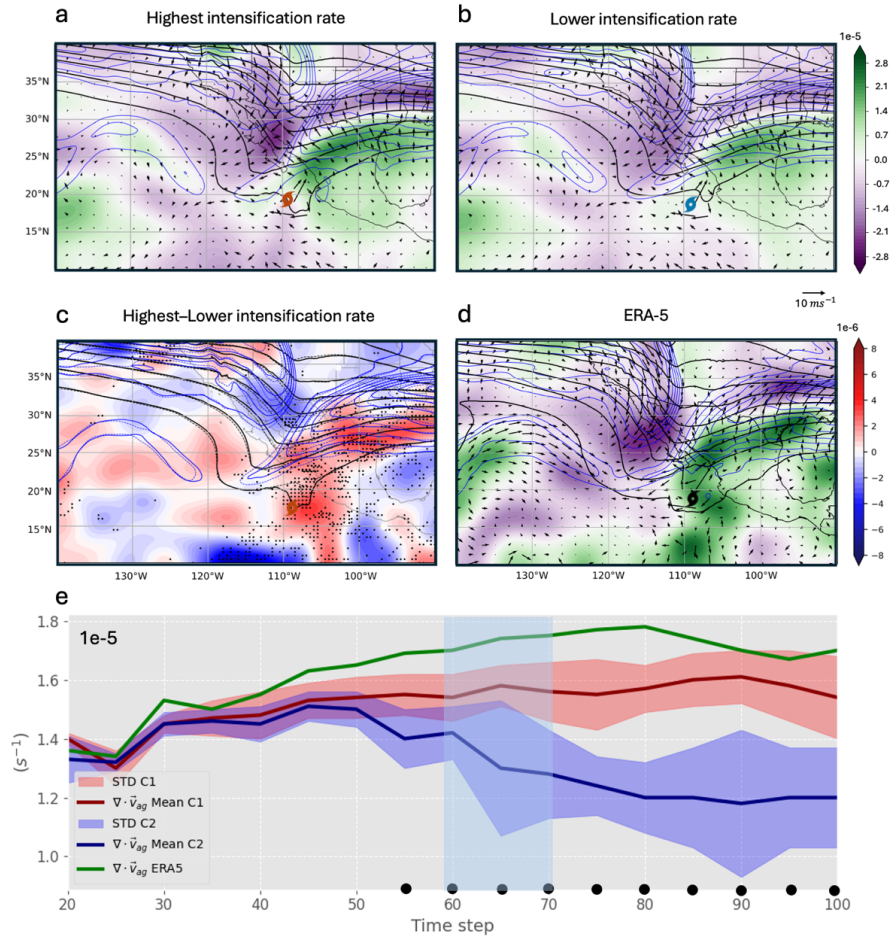
Figure 6. $\nabla \cdot \vec{V}_{ag}$-Composite (shaded; s^{-1}), jet stream (blue contours at 10 ms^{-1} intervals) and Z at 250 hPa (black contours at 20 m intervals) of (a) P_{80}, (b) P_{20} IRG (c) $P_{80} - P_{20}$ of $\nabla \cdot \vec{V}_{ag}$ (shaded; dots indicated statistical significance), solid (dashed) contour represent Z of P_{80} (P_{20}) IRG, and (d) same for ERA5 data. e) $\nabla \cdot \vec{V}_{ag}$ Temporal evolution calculated within a radial range of 500 km at 250 hPa, with the red (blue) line representing the higher (lower) IRG. The red (blue) shaded regions indicate the STD for the highest (lower) IRG and dots indicate statistical significance.

Figure 6e reveals distinct differences in the evolution of ageostrophic divergence between the two ensemble groups. The P_{80} group shows consistently higher values of ageostrophic divergence, particularly between +50 and +75 h, coinciding with Lidia's RI period. In contrast, the P_{20} group exhibits lower and declining values during this period, indicating weaker dynamical forcing. ERA5 closely follows the P_{80} pattern, supporting the physical credibility of the ensemble signal. These results highlight the role of upper-level divergence and jet-induced ascent in supporting RI in the P_{80} ensemble.

15

427

428   According to the quasi-geostrophic theory, regions with positive (negative) vorticity
429   advection are associated with upward (downward) vertical motions (Bluestein, 1992). In
430   Figures 7a and 7b, $\vec{V} \cdot \nabla(\vec{\xi} + f)$ is associated with a trough configuration, depicting
431   predominant positive (negative) values in front (behind) of the trough axis. In the same way,
432    $\vec{V} \cdot \nabla(\vec{\xi} + f)$ shows stronger and statistically significant positive values near Lidia's position
433   in P_{80} compared to P_{20}-ensemble (Fig. 7c); in addition, a branch with positive vorticity
434   advection values around Lidia is only identified in P_{80}-ensemble, and similar to ERA5 (Fig.
435   7d). The above is consistent with the greater proximity of the trough to Lidia in P_{80}-
436   ensemble, highlighting a more intense cyclonic vorticity advection over Lidia (also at earlier
437   time steps; not shown). Therefore, the trough-TC interaction is more robust in P_{80} than in
438   P_{20} as indicated earlier with the EFC metric. This finding shows that a mid-level trough can
439   facilitate the development of a moist layer (Wu et al., 2015), contributing to Lidia
440   intensification.

441

442
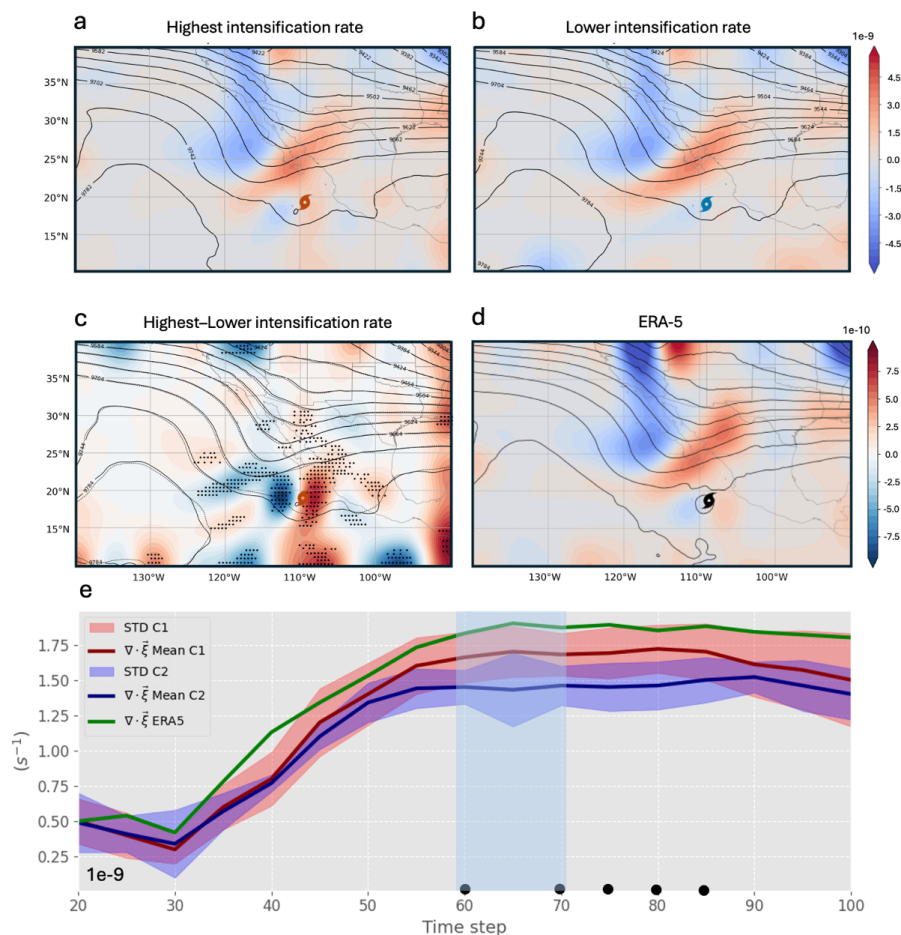
443   Figure 7. $\vec{V} \cdot \nabla(\vec{\xi} + f)$-Composite (shaded; s^{-2}) and Z at 300 hPa (black contours at 20 m
444   intervals) of (a) the P_{80} (b) P_{20} IRG, (c) $P_{80} - P_{20}$ (shaded; dots indicated statistical
445   significance), solid (dashed) contour represent Z of P_{80} (P_{20}) IRG and (d) same for ERA5 data.
446   e) $\vec{V} \cdot \nabla(\vec{\xi} + f)$ Temporal evolution calculated within a radial range of 500 km at 500 hPa,
447   with the red (blue) line representing the higher (lower) IRG. The red (blue) shaded regions
448   indicate the STD for the highest (lower) IRG and dots indicate statistical significance.

449

450   Figure 7e confirms the stronger vorticity forcing in the P_{80}-ensemble throughout Lidia's
451   intensification period. From time step +40 h onward, the P_{80} group exhibits consistently
452   higher values of vorticity advection, peaking near the RI window (+55 to +70 h), while the
453   P_{20} group remains consistently weaker, with little variability. The ERA5 line again follows the
454   P_{80} trajectory, supporting the robustness of the dynamical signal. The statistically significant
455   differences suggest that enhanced cyclonic vorticity advection, likely associated with the
456   trough's mid-level deformation, played a crucial role in promoting upward motion and
457   intensification in the P_{80}-ensemble.

458

459   The Q field in the P_{80}-ensemble (Fig. 8a) shows a more intense upward forcing in the
460   right region of the trough and extending to the divergence zone at the right entrance of the
461   jet streak in comparison to P_{20} Q values (Fig. 8b). This contrast becomes even more evident
462   when considering only RI members within P_{80}-ensemble(Figs. 9) are selected and reinforces
463   the idea of the influence of the trough in Lidia's RI. Based on Eq. (3), negative values of the
464   forcing term Q correspond to regions of upward vertical motion induced by vorticity
465   advection via the thermal wind (Dostalek, 2012). The areas surrounding Lidia are strongly
466   influenced by the dynamical forcing induced by the trough and the jet streak in the P_{80}-
467   ensemble (Fig. 8c). This result is further supported by the ERA5 reanalysis data (Fig. 8d),
468   which reveals a Q pattern similar to that observed in the P_{80}-ensemble, but with greater
469   intensity (note that ERA5 is only a member, not a composite group). In the absence of
470   substantial thermodynamic differences (Figs. 2 and 3), these results highlight the dominant
471   role of dynamic interaction between the trough, the jet streak, and the cyclone during RI.
472   These findings are particularly relevant for operational forecasting, also demonstrating the
473   capability of the ECMWF EPS to simulate Lidia's RI, even under complex extratropical
474   interactions influences.

475

476   The temporal evolution of the Trenberth forcing (Fig. 8e) reveals a clear and consistent
477   signal in the P_{80}-ensemble, with significantly more negative values, indicative of stronger
478   synoptic-scale upward motion. This enhanced forcing begins well before the onset of Lidia's
479   RI, peaking between +50 and +70 h. This temporal analysis supports a causal interpretation:
480   the dynamical forcing precedes and facilitates the RI process, rather than being a
481   consequence of it. In contrast, the P_{20} group shows much weaker and less coherent values
482   throughout, indicating and absence of favorable dynamical support for RI.
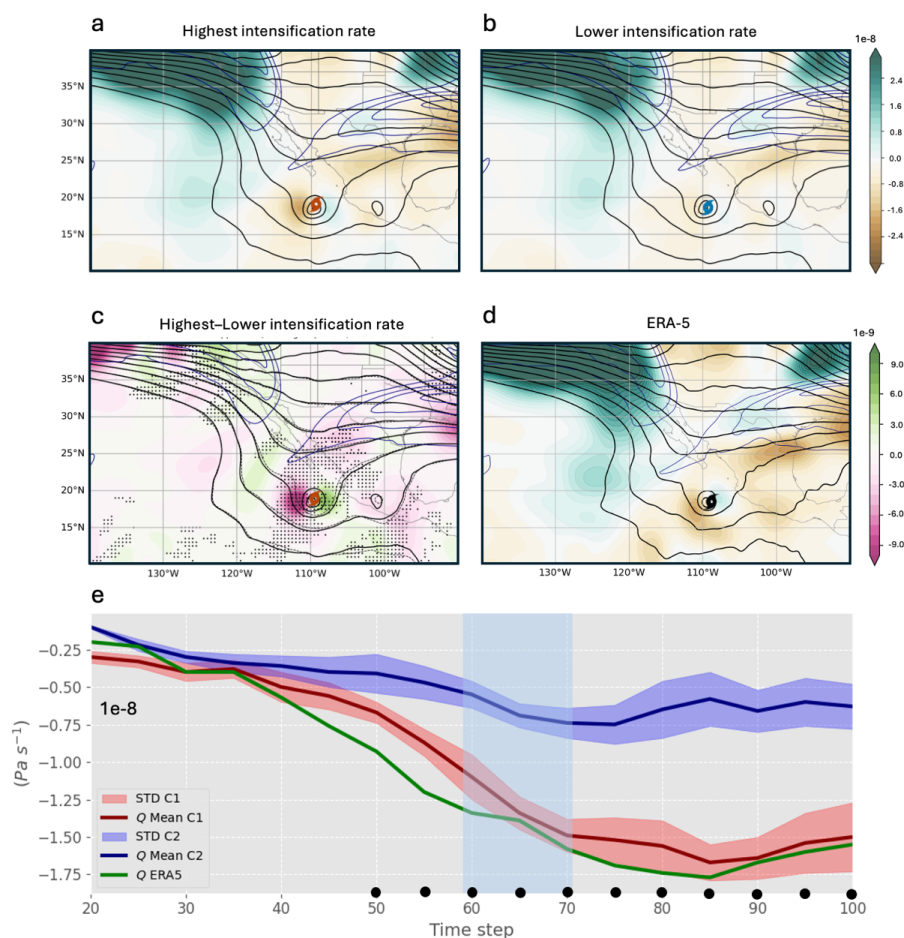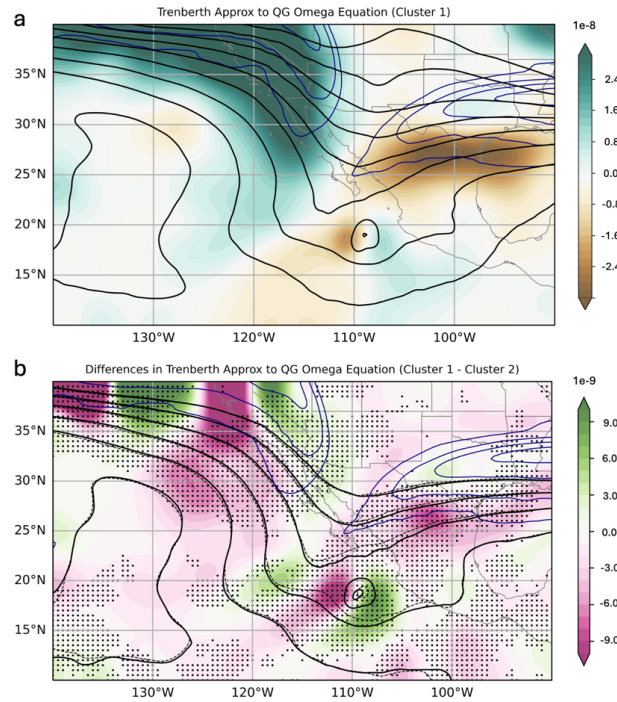
483

484

Figure 8. Q-Composite (shaded; $Pa \cdot s^{-1}$) at 500 hPa, jet stream (blue contours at $10\ m\ s^{-1}$
intervals) at 250 hPa and Z at 500 hPa (black contours at 20 m intervals) of (a) the P_{80} (b)
P_{20} IRG, (c) $P_{80} - P_{20}$ of Q (shaded; dots indicated statistical significance), solid (dashed)
contour represent Z of P_{80} (P_{20}) IRG and (d) same for ERA5 data. (e) Q Temporal evolution
calculated within a radial range of 500 km at 500 hPa, with the red (blue) line representing
the higher (lower) IRG. The red (blue) shaded regions indicate the STD for the highest (lower)
IRG and dots indicate statistical significance.

In P_{80}-ensemble, the trough is broader (≈300 km) and positioned closer to Lidia (around
500 km; Figs. 3a, b), in agreement with previous studies showing that favorable trough–TC
interactions occur when the trough lies to the northwest at an optimal distance (Hanley et
al., 2001). Significant differences are observed in both the amplitude and distance relative
to Lidia (Fig. 2c). A similar pattern has been noted in some Atlantic basin cases (Hanley et
al., 2001; Fischer et al., 2019; Sato et al., 2020), where effective trough–TC interactions are
facilitated by a favorable distance, typically between 500-1000 km. Fischer et al. (2019) also
found in a climatological study that TCs in the North Atlantic tend to intensify more rapidly

501 when the trough is positioned to the northwest, more closely resembling the trough–Lidia
502 pattern in the RI group (Fig. 3a) than in the non-RI group in this work (Fig. 3b).
503

505 Figure 9. (a) Composite of Trenberth forcing (shaded; $Pa \cdot s^{-1}$) at 500 hPa, jet stream (blue
506 contours at $10\ m\ s^{-1}$ intervals) at 250 hPa and geopotential height at 500 hPa (black
507 contours at 20 m intervals) of RI members, (b) Trenberth forcing (shaded) differences (P_{80}-
508 RI members minus P_{20}; dots indicated statistical significance), solid (dashed) contour
509 represent geopotential height of RI group.

510

511   These findings further support the hypothesis that dynamical forcing triggered Lidia's
512 RI. In the P_{80}-ensemble the trough is broader (~ 300 km) and closer to Lidia (~500 km; Figs.
513 10a, b). Evident differences are observed in both the amplitude and distance relative to Lidia
514 (Fig. 10c). A similar configuration has been noted in some Atlantic basin cases (Hanley et al.,
515 2001; Fischer et al., 2019; Sato et al., 2020), where effective trough–TC interactions require
516 a favorable distance. This configuration is associated with different behavior of $\vec{V}_{irr}$ at upper-
517 levels (Figs. 10d-f), where the proximity of the trough's divergence zone enhances
518 ventilation in the P_{80}-ensemble (Fig. 10d) with significant $\vec{V}_{irr}$ differences reaching ~$4\ m s^{-1}$
519 to the west-northwest of Lidia. Consequently, the superposition of both divergence zones
520 amplifies the upper-level anticyclonic circulation, consistent with increasing EFC values in
521 P_{80} toward Lidia (Fig. 5) strengthens upward motion and enabling RI.
522

523   On the other hand, the VWS remains moderate around Lidia's center in both ensemble
524   groups, with values between 10-15 ms^{-1} during RI period (Fig. 10g, h). Slightly higher VWS
525   values are observed to the south of Lidia. To the west and near of Lidia center, VWS values
526   are higher in P_{80}-ensemble (around $\sim 5\ ms^{-1}$; Fig. 10i), though still within favorable ranges
527   for intensification (Sharma and Varma, 2022). In contrast, regions beyond 2° radial distance
528   in P_{80}-ensemble show significantly lower VWS values, consistent with the position and
529   shape of the jet stream. In P_{20}-ensemble, a stronger jet stream is present north of Lidia,
530   resulting in a more significant increase in VWS compared to P_{80}-ensemble. Thus, the
531   position and intensity of the jet streak relative to Lidia's position could potentially limit its
532   intensification in P_{20}-ensemble.

533

534   The results suggest that the upward motions induced by dynamical mechanisms
535   associated with Lidia's interaction with a trough are consistent with the greater RH in P_{80},
536   particularly near the center of Lidia and in the southern region where the trough appears to
537   enhance its influence (Figs. 10j–l). This region coincides with the trough-cyclone interaction,
538   where vertical motions are strongly driven by dynamical forcing. The analyzed atmospheric
539   patterns, including the dynamical forcing associated with the trough and jet streak, suggest
540   that higher RH in P_{80} may be linked to increased condensation rates during air ascents
541   around center of Hurricane Lidia, leading to core warming (Emanuel, 1986; Zhang et al.,
542   2013; Zhang and Emanuel, 2016). This scenario could also decrease VWS, further promoting
543   Lidia's RI. These findings align with previous studies (Qiu et al., 2020) indicating that TC
544   intensification can occur even under moderate to high VWS provided that the surrounding
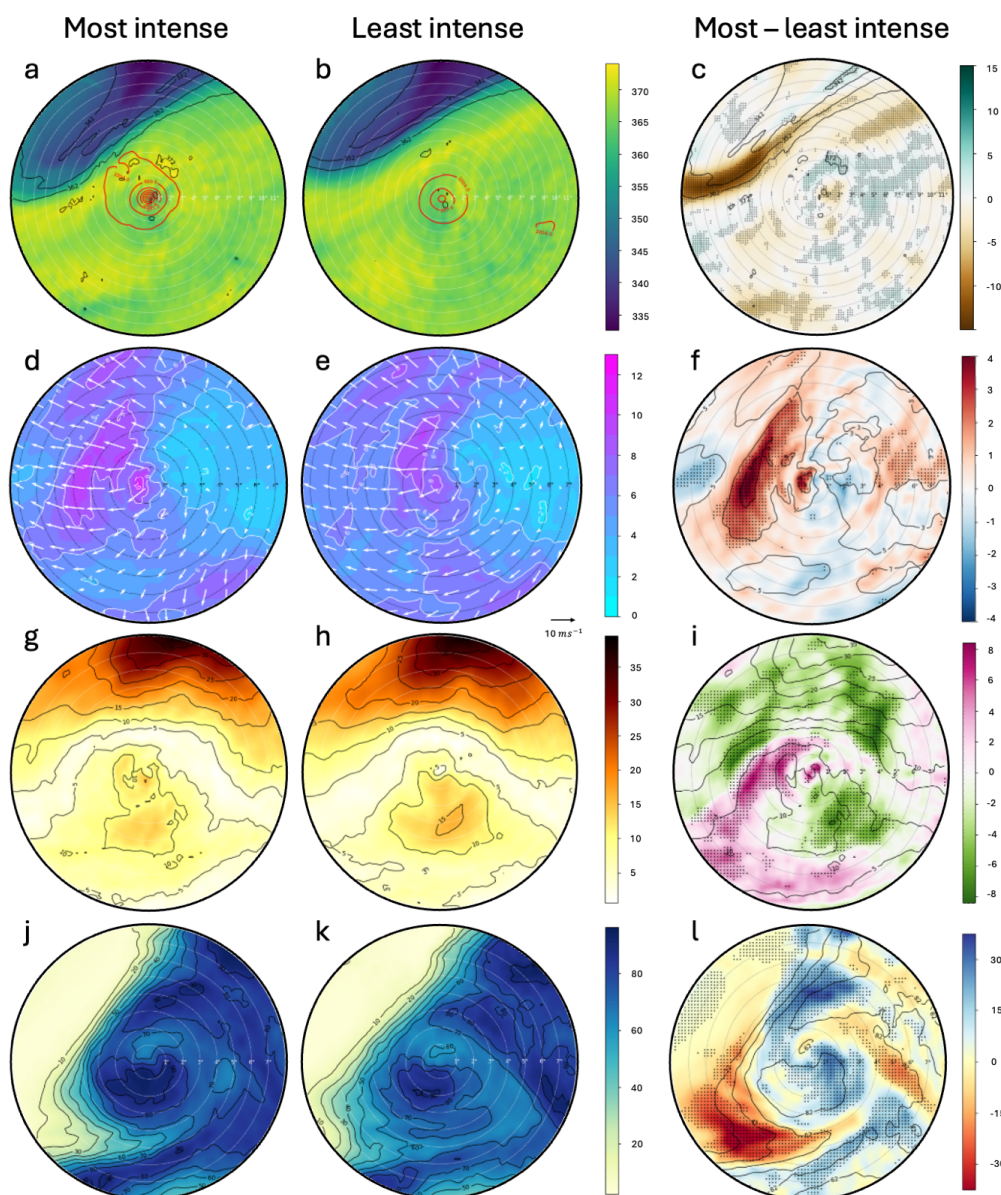545   layer remains sufficiently moist.

546

Figure 10. SCC for the time step 55-h of: θ (K) at 1.5 PVU for (a) P_{80}, (b) P_{20} IRG, and (c) $P_{80} - P_{20}$ IRG, red contours are MSPL; $\left|\vec{V}_{irr}\right|$ $(m\,s^{-1})$, at 200 hPa for (d) P_{80}, (e) P_{20} IRG, and (f) $P_{80} - P_{20}$ IRG; VWS $(m\,s^{-1})$ for (g) P_{80}, (h) P_{20} IRG and (i) $P_{80} - P_{20}$ IRG, and RH (%) (j) P_{80}, (k) P_{20} IRG and (l) $P_{80} - P_{20}$ IRG at 500 hPa.

While previous studies (Braun and Tao, 2000; Rios-Berríos et al., 2018) have shown that increased mid-level humidity can play a key role in RI. The current results indicate that the

556   RH differences between the P_{80} and P_{20} ensembles are minimal and statistically
557   insignificant. This suggests that RH was not the primary driver of RI in this event. Instead,
558   the P_{80} ensemble is characterized by early and sustained dynamic forcing, particularly the
559   strong negative Trenberth forcing observed before the RI onset, which likely initiated
560   upward motion and enhanced upper-level ventilation near the storm core. This synoptic-
561   scale ascent, coupled with the release of latent heat, contributed to a favorable adjustment
562   of the potential vorticity structure in the upper troposphere, reinforcing the outflow and
563   aiding in the vertical alignment of the vortex. As a result of the PV vertical redistribution, a
564   gradual reduction in VWS is observed in the P_{80} group. This reduction is related to higher
565   Trenberth forcing, supporting a causal sequence in which synoptic-scale forcing
566   preconditions, such as strong convection and vortex alignment, subsequently amplify this
567   favorable state, accelerating the intensification process (Chen and Gopalakrishnan, 2019;
568   Komaromi and Doyle, 2018; Stevenson et al., 2014). Figure 11 confirms this evolution:
569   stronger divergence and PV anomalies emerge after the initial forcing, aligning with the
570   onset of RI. The combined evidence supports the conclusion that in the case of Hurricane
571   Lidia, RI was dynamically triggered by the interaction with the upper-level trough and jet
572   stream, with thermodynamic factors, such as PI, SST and RH, playing a secondary, and
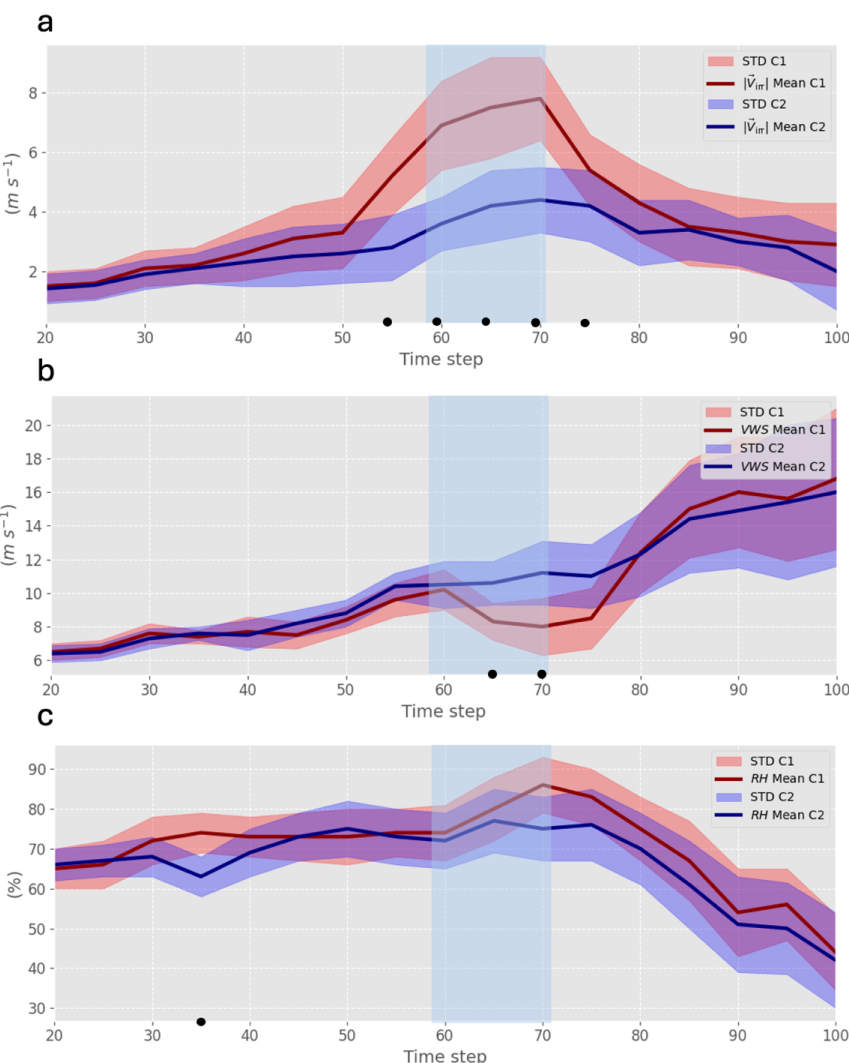573   permissive, rather than a decisive, role.

574
575   Figure 11. Time evolution of (a) ageostrophic wind at 250 hPa, (b) VWS (850–200 hPa), and
576   (c) mid-level RH (700–500 hPa) within 500 km of Lidia. Red (blue) lines show the mean for
577   the higher (lower) IRG; shaded areas indicate STD. Light blue band indicate the RI period.
578   Black dots denote significant differences.
579

580   **4   Summary and conclusions**
581

582   This research presents a novel examination of the interaction between a mid- and
583   upper-level trough and Hurricane Lidia in the northeastern Pacific, a region where studies
584   are less frequent compared to the Atlantic basin, particularly regarding RI. Since
585   thermodynamic factors such as PI and SST do not seem to explain the differences observed
586   between the members of the group in the intensification of Lidia, some dynamic variables

587   associated with forcings more typical of higher latitudes are analyzed, which usually appear
588   in the autumn months in subtropical areas of the northeastern Pacific coasts (DiMego et al.,
589   1976).

590

591   Based on previous work in the Atlantic basin (Fischer et al., 2019), which demonstrated
592   that tropical cyclones experiencing RI often coincide with the presence of an upper-level
593   trough approaching from the northwest at an optimal distance, our study expands this
594   framework by demonstrating for the first time a similar dynamic configuration driving RI in
595   the northeastern Pacific. By analyzing synoptic dynamical indicators, such as the Trenberth
596   forcing, ageostrophic wind divergence and vorticity advection, we demonstrate how these
597   dynamical processes play a crucial role in Lidia's RI. The EFC values greater than 10
598    $ms^{-1}day^{-1}$ in the P_{80}-ensemble indicate the trough-TC interaction during the RI period,
599   reinforcing the critical role of the trough in enhancing vertical motions and upper-level
600   ventilation. In a context where ocean temperatures are rising and an increasing trend in RI
601   hurricane frequency has been documented (Majumdar et al., 2023; Li et al., 2023), this
602   work provides the first case study of trough-TC interaction leading to RI in the northeastern
603   Pacific, highlighting the increased proximity and breadth of the trough near Lidia a key driver
604   of its RI. Unlike Fischer et al. (2019), who focused on climatological composites and
605   individual case diagnostics in the Atlantic, this study provides a probabilistic ensemble-
606   based assessment linked to dynamic forcings under realistic forecast uncertainty conditions.

607

608   The obtained results underscore the role of dynamical mechanisms, analyzed through
609   quasi-geostrophic forcing, in triggering significant upward vertical motions that contribute
610   to the Lidia's RI. These dynamics are evident in the P_{80}-ensemble (even more evident in RI
611   members), where Lidia undergoes RI, showing stronger ageostrophic wind divergence,
612   enhanced vorticity advection at mid- and upper-levels, and more pronounced Trenberth
613   forcing, all associated with the influence of the trough. In contrast, in the P_{20}-ensemble,
614   Lidia does not interact with the trough and experiences less favorable conditions. The
615   proximity and intensity of a jet stream to Lidia's north increase in VWS, which limited the
616   potential for intensification.

617

618   The enhanced Trenberth forcing in the P_{80} ensemble appears several hours before the
619   onset of RI, indicating that synoptic-scale ascent likely preconditioned the environment
620   rather than resulting from the intensification itself. This timing supports a causal
621   interpretation in which the large-scale forcing drives changes within the TC. Following this
622   initial dynamic trigger, latent heat release near the cyclone core contributed to a favorable
623   upper-level PV redistribution. This adjustment likely enhanced the upper outflow layer and
624   contributed to the subsequent reduction in VWS observed in the P_{80} group, further
625   amplifying the intensification process.

626

627   In contrast, relative humidity differences between the two ensembles were small and
628   not statistically significant, suggesting that moisture availability was not a limiting factor in
629   this case. While previous studies (Braun & Tao, 2000; Ríos-Berríos et al., 2018) have shown

630 that enhanced mid-level moisture can favor RI, our results indicate that it played a secondary
631 role here, acting more as a permissive background condition than an active driver.
632
633 By demonstrating the effectiveness of EPS-ECMWF in capturing complex trough-TC
634 interactions, this study highlights the critical role of EPS as an indispensable tool for
635 operational forecasting in the northeastern Pacific, especially along the Pacific coast of
636 Mexico. EPS are particularly valuable for quantifying uncertainty in RI scenarios, which
637 remain challenging to predict due to the complex dynamical and thermodynamical
638 processes involved. The present results show that EPS can successfully differentiate
639 between dynamically favorable and unfavorable environments, even in a context where
640 high-resolution operational models are not readily available, as is often the case in Mexico.
641 This makes EPS-based diagnostics especially useful for forecasters operating in data-sparse
642 or resource-limited settings. In this region, during autumn months, the subtropical jet
643 stream frequently interacts with TCs, increasing the likelihood of dynamical forcing
644 mechanisms that can either enhance or inhibit intensification.
645
646 This study illustrates how broader and deeper mid-level troughs, such as the one
647 observed at 500 hPa in Hurricane Lidia, can significantly enhance vertical motion and upper-
648 level ventilation conducive to RI. Operationally, diagnostic tools such as Trenberth forcing
649 and EFC metric could be integrated into forecasting to better assess trough-TC interactions.
650 Measuring these variables in real time would provide forecasters with actionable insights
651 into the likelihood of RI, particularly when TCs recurve toward the densely populated Pacific
652 coast of Mexico. Although the limitations of a single case study are evident, we suspect that
653 other RIs in the northeastern Pacific have been influenced by similar dynamical
654 mechanisms. However, while our results offer robust evidence from a synoptic-scale
655 perspective, this study is based on a single case. Future research should expand this
656 methodology to a broader set of events and explore complementary approaches using
657 convection-permitting high-resolution simulations. Such simulations would help resolve
658 inner-core processes and mesoscale interactions that were intentionally simplified in this
659 study, which focused on evaluating large-scale dynamical forcings. In this regard, the
660 framework proposed here serves as a cost-effective, scalable strategy to support RI
661 forecasting in regions with limited access to high-resolution modeling systems and highlights
662 the continued need to refine multi-scale diagnostic techniques for better understanding and
663 prediction of TC intensification. Also, expanding this methodology to a broader set of cases
664 could offer a more comprehensive understanding of trough-TC interactions and their role in
665 RI, ultimately improving operational forecasting capabilities in this understudied region.
666
667 **Declaration of Competing Interest**
668
669 The authors declare no conflicts of interest relevant to this study.
670
671 **Acknowledgments**

678 **Open Research**
679
680 The tracking data for Hurricane Lidia can be found in López-Reyes, M. (2024). Atmospheric
681 data sets can be accessed through the MARS database, hosted by ECMWF, at
682 https://confluence.ecmwf.int/display/MARS. Additionally, ERA-5 reanalysis data base is
683 allowed in Climate Data Store (CDS; available at https://climate.copernicus.eu/climate-
684 reanalysis).
685
686 **Author contributions**
687
688 Conceptualization: MLR, MLMP, JJGA. Methodology: MLR, MLMP, CCS, JJGA. Project
689 administration: MLMP. Supervision: MLPM, CCS, JJGZ. Writing-original draft: MLR. Writing-
690 review and edits: MLR, MLMP, CCS, JJGA.
691

692 **References**
693
694 Avila, L. A., 1998: Forecasting tropical cyclone intensity changes: An operational
695 challenge. Preprints, *Symp. on Tropical Cyclone Intensity Change,* Phoenix, AZ, Amer.
696 Meteor. Soc., 1–3.

697 Billingsley, D. (1998). A review of QG theory—Part III: A different approach. *Natl. Wea.
698 Dig*, *22*, 3-10.

699 Bister, M., & Emanuel, K. A. (2002). Low frequency variability of tropical cyclone potential
700 intensity 1. Interannual to interdecadal variability. *Journal of Geophysical Research:
701 Atmospheres*, *107*(D24), ACL-26. https://doi.org/10.1029/2001JD000776

702 Bluestein, H. B. (1992). *Synoptic-dynamic Meteorology in Midlatitudes: Observations and
703 theory of weather systems* (Vol. 2). Taylor & Francis.

704 Bracken, W. E., & Bosart, L. F. (2000). The Role of Synoptic-Scale Flow during Tropical
705 Cyclogenesis over the North Atlantic Ocean. *Monthly Weather Review*, *128*(2), 353-
706 376. https://doi.org/10.1175/1520-0493(2000)128<0353:TROSSF>2.0.CO;2

707 Braun, S. A., & Tao, W.-K. (2000). Sensitivity of high-resolution simulations of Hurricane Bob
708 (1991) to planetary boundary layer parameterizations. Monthly Weather Review, 128(12),
709 3941–3961. https://doi.org/10.1175/1520-0493(2000)129<3941:SOHRSO>2.0.CO;2

710   Callaghan, J. (2020). WITHDRAWN: The interaction of Hurricane Michael with an upper
711   trough leading to intensification right up to landfall. *Tropical Cyclone Research and*
712   *Review*, *9*(2), 135-142. https://doi.org/10.1016/j.tcrr.2019.07.009

713   Cao, J., Ran, L., & Li, N. (2014). An Application of the Helmholtz Theorem in Extracting the
714   Externally Induced Deformation Field from the Total Wind Field in a Limited Domain.
715   Monthly Weather Review, 142(5), 2060-2066. https://doi.org/10.1175/MWR-D-13-00311.1

716   Carrasco, C., Landsea, C., & Lin, Y. (2014). The influence of tropical cyclone size on its
717   intensification. Weather and Forecasting, 29, 582–590. https://doi.org/10.1175/WAF-D-13-
718   00092.1

719   Chen, H. & Gopalakrishnan, S. G. (2015). *A study on the asymmetric rapid intensification of*
720   *Hurricane Earl (2010) using the HWRF system*. Journal of the Atmospheric Sciences, *72*(2),
721   531–550. https://doi.org/10.1175/JAS-D-14-0097.1

722   Chen, X., Zhang, J. A., & Marks, F. D. (2019). A thermodynamic pathway leading to rapid
723   intensification of tropical cyclones in shear. *Geophysical Research Letters*, *46*(15), 9241-
724   9251. https://doi.org/10.1029/2019GL083667

725   Chen, Y., Gao, S., Li, X., & Shen, X. (2021). Key environmental factors for rapid intensification
726   of the South China Sea tropical cyclones. *Frontiers in Earth Science*, *8*, 609727.
727   https://doi.org/10.3389/feart.2020.609727

728   Chorin, A. J., Marsden, J. E., & Marsden, J. E. (1990). A mathematical introduction to fluid
729   mechanics (Vol. 3, pp. 269-286). New York: Springer.

730   Collins, Clarence, Tyler Hesser, Peter Rogowski, and Sophia Merrifield. (2021). "Altimeter
731   Observations of Tropical Cyclone-generated Sea States: Spatial Analysis and Operational
732   Hindcast Evaluation" *Journal of Marine Science and Engineering* 9, no. 2: 216.
733   https://doi.org/10.3390/jmse9020216

734   DeMaria, M., Franklin, J. L., Onderlinde, M. J., & Kaplan, J. (2021). Operational forecasting
735   of tropical cyclone rapid intensification at the National Hurricane Center. *Atmosphere*, *12*(6),
736   683. https://doi.org/10.3390/atmos12060683

737   DeMaria, M., J. Kaplan, and J. Baik, 1993: Upper-Level Eddy Angular Momentum Fluxes and
738   Tropical   Cyclone   Intensity   Change. *J.   Atmos.   Sci.*, **50**,   1133–
739   1147, https://doi.org/10.1175/1520-0469(1993)050<1133:ULEAMF>2.0.CO;2.

740   DiMego, G. J., Bosart, L. F., & Endersen, G. W. (1976). An Examination of the Frequency and
741   Mean Conditions Surrounding Frontal Incursions into the Gulf of Mexico and Caribbean
742   Sea. *Monthly   Weather   Review*, *104*(6),   709-718. https://doi.org/10.1175/1520-
743   0493(1976)104<0709:AEOTFA>2.0.CO;2

744   Dostalek, J. F., Schubert, W., DeMaria, M., Estep, D., Johnson, R., & Vonder Haar, T. (2012).
745   Global omega equation: Derivation and application to tropical cyclogenesis in the North
746   Atlantic Ocean.

747   Emanuel, K. A., & Lin, J. (2024, May). Hurricane Otis: A case for a rapid migration toward
748   probabilistic tropical cyclone forecasting. Paper presented at the 36th Conference on
749   Hurricanes and Tropical Meteorology, American Meteorological Society.
750
751   Emanuel, K. A. (1986). An Air-Sea Interaction Theory for Tropical Cyclones. Part I: Steady-
752   State   Maintenance. *Journal   of   Atmospheric   Sciences*, *43*(6),   585-
753   605. https://doi.org/10.1175/1520-0469(1986)043<0585:AASITF>2.0.CO;2
754
755   Emanuel, K. A. (1988). The maximum intensity of hurricanes. *J. Atmos. Sci.* 45, 1143–1155.
756   doi:10.1175/1520-0469(1988)045<1143:tmioh>2.0.co;2

757   Fischer, M. S. (2018). Tropical cyclone rapid intensification in environments of upper-
758   tropospheric troughs: Environmental influences and convective characteristics (Order No.
759   10839442).   Available   from   ProQuest   One   Academic.   (2087658194).   Retrieved   from
760   http://wdg.biblio.udg.mx:2048/login?url=https://www.proquest.com/dissertations-
761   theses/tropical-cyclone-rapid-intensification/docview/2087658194/se-2

762   Fischer, M. S., Tang, B. H., & Corbosiero, K. L. (2019). A Climatological Analysis of Tropical
763   Cyclone Rapid Intensification in Environments of Upper-Tropospheric Troughs. Monthly
764   Weather Review, 147(10), 3693-3719. https://doi.org/10.1175/MWR-D-19-0013.1

765   García-Franco, J. L., Gómez-Ramos, O., & Domínguez, C. (2024). Hurricane Otis: the costliest
766   and   strongest   hurricane   at   landfall   on   record   in   Mexico. *Weather*, *79*(6),   182-184.
767   https://doi.org/10.1002/wea.4555

768   Gilford, D. M. (2021). pyPI (v1. 3): Tropical cyclone potential intensity calculations in
769   Python. *Geoscientific Model Development*, *14*(5), 2351-2369. https://doi.org/10.5194/gmd-
770   14-2351-2021
771
772   Hanley, D., Molinari, J., & Keyser, D. (2001). A composite study of the interactions between
773   tropical cyclones and upper-tropospheric troughs. *Monthly weather review*, *129*(10), 2570-
774   2584. https://doi.org/10.1175/1520-0493(2001)129<2570:ACSOTI>2.0.CO;2

775   Heming, J. T., Prates, F., Bender, M. A., Bowyer, R., Cangialosi, J., Caroff, P., ... & Xiao, Y. (2019).
776   Review   of   recent   progress   in   tropical   cyclone   track   forecasting   and   expression   of
777   uncertainties. *Tropical   Cyclone   Research   and   Review*, *8*(4),   181-218.
778   https://doi.org/10.1016/j.tcrr.2020.01.001

779   Hersbach, H., Bell, B., Berrisford, P., Hirahara, S., Horányi, A., Muñoz-Sabater, J., ... &
780   Thépaut, J. N. (2020). The ERA5 global reanalysis. *Quarterly Journal of the Royal*
781   *Meteorological Society*, *146*(730), 1999-2049. https://doi.org/10.1002/qj.3803

782   Hu, Yanyang, and Xiaolei Zou. (2021). "Tropical Cyclone Center Positioning Using Single
783   Channel Microwave Satellite Observations of Brightness Temperature" *Remote Sensing* 13,
784   no. 13: 2466. https://doi.org/10.3390/rs13132466

785   J.P. Cangialosi (2018). The State of Hurricane Forecasting. National Hurricane Center Blog–
786   Inside   the   Eye.   https://noaanhc.wordpress.com/2018/03/09/the-state-of-
787   hurricaneforecasting

788   Jin, R., Li, Y., Chen, X., & Li, M. (2023). Characteristics of the upper-level outflow and its
789   impact on the rapid intensification of Typhoon Roke (2011). *Frontiers in Earth Science*, *10*,
790   1021308. https://doi.org/10.3389/feart.2022.1021308

791   Kaplan, J., & DeMaria, M. (2003). Large-scale characteristics of rapidly intensifying tropical
792   cyclones in the North Atlantic basin. *Weather and forecasting*, *18*(6), 1093-1108.
793   https://doi.org/10.1175/1520-0434(2003)018<1093:LCORIT>2.0.CO;2

794   Komaromi, W. A., & Doyle, J. D. (2018). On the dynamics of tropical cyclone and trough
795   interactions. *Journal of the Atmospheric Sciences*, *75*(8), 2687-2709.
796   https://doi.org/10.1175/JAS-D-17-0272.1

797   Larson, J., Zhou, Y., & Higgins, R. W. (2005). Characteristics of landfalling tropical cyclones in
798   the United States and Mexico: Climatology and interannual variability. *Journal of*
799   *Climate*, *18*(8), 1247-1262. https://doi.org/10.1175/JCLI3317.1

800   Ling, S., Lu, R., & Cao, J. (2025). The variation in tropical cyclone genesis over the western
801   North Pacific during the El Niño summers. Climate Dynamics, 63(1), 13.
802   https://doi.org/10.1007/s00382-024-07484-9

803   López Reyes, M., & Meulenert, A. (2021). Comparación de las variables físicas que influyen
804   en la rápida intensificación de los ciclones tropicales del Océano Pacífico nororiental durante
805   el   periodo   1970-2018. *Cuadernos Geográficos*, *60*(2),   105-125.
806   https://doi.org/10.30827/cuadgeo.v60i2.15474

807   López-Reyes, M., Gónzalez-Alemán, J. J., Calvo-Sancho, C., Bolgiani, P., Sastre, M., & Martín,
808   M. L. (2024). Remote Interactions between tropical cyclones: The case of Hurricane Michael
809   and Leslie's high predictability uncertainty. *Atmospheric Research*, 107697.
810   https://doi.org/10.1016/j.atmosres.2024.107697

811   Loughe, A. F., Lai, C., & Keyser, D. (1995). A Technique for Diagnosing Three-Dimensional
812   Ageostrophic Circulations in Baroclinic Disturbances on Limited-Area Domains. Monthly
813   Weather   Review,   123(5),   1476-1504.   https://doi.org/10.1175/1520-
814   0493(1995)123<1476:ATFDTD>2.0.CO;2

815   Luna-Niño, R., Cavazos, T., Torres-Alavez, J. A., Giorgi, F., & Coppola, E. (2021). Interannual
816   variability of the boreal winter subtropical jet stream and teleconnections over the CORDEX-

817   CAM domain during 1980–2010. *Climate Dynamics*, *57*(5), 1571-1594.
818   https://doi.org/10.1007/s00382-020-05509-7

819   Mann, H. B., & Whitney, D. R. (1947). On a Test of Whether one of Two Random Variables is
820   Stochastically Larger than the Other. *The Annals of Mathematical Statistics*, *18*(1), 50–60.
821   http://www.jstor.org/stable/2236101

822   Molinari, J., & Vollaro, D. (1990). External influences on hurricane intensity. Part II: Vertical
823   structure and response of the hurricane vortex. *Journal of the Atmospheric sciences*, *47*(15),
824   1902-1918. https://doi.org/10.1175/1520-0469(1990)047<1902:EIOHIP>2.0.CO;2

825   Richard J. Pasch (2024). Hurricane Milton Discussion Number 12 (Report). National
826   Hurricane Center. Archived from the original on October 9, 2024. Retrieved October
827   7, 2024.

828   Richard J. Pasch (October 7, 2024). Tropical Cyclone Report: Hurricane Lidia (EP152023).
829   National Hurricane Center. https://www.nhc.noaa.gov/data/tcr/EP152023_Lidia.pdf

830   Peirano, C. M., Corbosiero, K. L., & Tang, B. H. (2016). Revisiting trough interactions and
831   tropical cyclone intensity change. *Geophysical Research Letters*, *43*(10), 5509-5515.
832   https://doi.org/10.1002/2016GL069040

833   Prasanth, S., Chavas, D. R., Marks Jr, F. D., Dubey, S., Shreevastava, A., & Krishnamurti, T. N.
834   (2020). Characterizing the energetics of vortex-scale and sub-vortex-scale asymmetries
835   during tropical cyclone rapid intensity changes. *Journal of the Atmospheric Sciences*, *77*(1),
836   315-336. https://doi.org/10.1175/JAS-D-19-0067.1.

837   RAMMB/CIRA Slider. (2024, October 1). GOES-16 visible satellite image. Retrieved from
838   https://rammb-slider.cira.colostate.edu/

839   Ríos-Berríos, R., Torn, R. D., & Davis, C. A. (2018). A closer look at the structure and intensity
840   changes of rapidly intensifying tropical cyclones. Monthly Weather Review, 146(11), 3625–
841   3645. https://doi.org/10.1175/MWR-D-18-0111.1

842   Ryglicki, D. R., Velden, C. S., Reasor, P. D., Hodyss, D., & Doyle, J. D. (2021). Observations of
843   Atypical Rapid Intensification Characteristics in Hurricane Dorian (2019). Monthly Weather
844   Review, 149(7), 2131-2150. https://doi.org/10.1175/MWR-D-20-0413.1

845   Sadler J. (1975). *The upper tropospheric circulation over the global tropics*. University
846   of Hawaii. Retrieved February 17, 2025, from
847   https://www.soest.hawaii.edu/Library/Sadler.html

848   Sato, K., Inoue, J., & Yamazaki, A. (2020). Performance of forecasts of hurricanes with and
849   without upper-level troughs over the mid-latitudes. *Atmosphere*, *11*(7), 702.
850   https://doi.org/10.3390/atmos11070702

851   Servicio Meteorológico Nacional. (2023, October 24). Special bulletin: Hurricane Otis rapid
852   intensification and landfall warning [PDF]. Comisión Nacional del Agua (CONAGUA), Mexico.
853   Retrieved   from
854   https://smn.cna.gob.mx/tools/DATA/Ciclones%20Tropicales/Resumenes/2023.pdf

855   Sharma, N., & Varma, A. K. (2022). Impact of vertical wind shear in modulating tropical
856   cyclones eye and rainfall structure. *Natural Hazards*, *112*(3), 2083-2100.
857   https://doi.org/10.1007/s11069-022-05257-3

858   Shi, D., & Chen, G. (2021). The implication of outflow structure for the rapid intensification
859   of tropical cyclones under vertical wind shear. *Monthly Weather Review*, *149*(12), 4107-
860   4127. https://doi.org/10.1175/MWR-D-21-0141.1

861   Shi, D., & Chen, G. (2023). Modulation of Asymmetric Inner-Core Convection on Midlevel
862   Ventilation Leading up to the Rapid Intensification of Typhoon Lekima (2019). *Journal of
863   Geophysical Research: Atmospheres*, *128*(7), e2022JD037952.
864   https://doi.org/10.1029/2022JD037952

865   Stevenson, S. N., Corbosiero, K. L., & Molinari, J. (2014). The Convective Evolution and Rapid
866   Intensification of Hurricane Earl (2010). Monthly Weather Review, 142(11), 4364-4380.
867   https://doi.org/10.1175/MWR-D-14-00078.1

868   Tan, Z. M., Lei, L., Wang, Y., Xu, Y., & Zhang, Y. (2022). Typhoon track, intensity, and structure:
869   From theory to prediction. *Adv. Atmos. Sci.* **39**, 1789–1799https://doi.org/10.1007/s00376-
870   022-2212-1

871   Tao, D., Van Leeuwen, P. J., Bell, M., & Ying, Y. (2022). Dynamics and predictability of tropical
872   cyclone rapid intensification in ensemble simulations of Hurricane Patricia (2015). *Journal
873   of Geophysical Research: Atmospheres*, *127*(8), e2021JD036079.
874   doi.org/10.1029/2021JD036079

875   Tong, B., Wang, X., Wang, D., & Zhou, W. (2023). A Novel Mechanism for Extreme El Niño
876   Events: Interactions between Tropical Cyclones in the Western North Pacific and Sea Surface
877   Warming in the Eastern Tropical Pacific. Journal of Climate, 36(8), 2585-2601.
878   https://doi.org/10.1175/JCLI-D-21-1014.1

879   Wang, Y., Li, Y., Xu, J., Tan, Z. M., & Lin, Y. (2021). The intensity dependence of tropical cyclone
880   intensification rate in a simplified energetically based dynamical system model. *Journal of
881   the Atmospheric Sciences*, *78*(7), 2033-2045. https://doi.org/10.1175/JAS-D-20-0393.1.

882   Wu, L., Su, H., Fovell, R. G., Dunkerton, T. J., Wang, Z., & Kahn, B. H. (2015). Impact of
883   environmental moisture on tropical cyclone intensification. Atmospheric Chemistry and
884   Physics, 15(24), 14041-14053. https://doi.org/10.5194/acp-15-14041-2015
885

886   Zhang, D. L., & Chen, H. (2012). Importance of the upper-level warm core in the rapid
887   intensification of a tropical cyclone. *Geophysical Research Letters*, *39*(2).
888   https://doi.org/10.1029/2011GL050578
889
890   Zhang, J. A., Rogers, R. F., Reasor, P. D., Uhlhorn, E. W., & Marks, F. D., Jr. (2013). Asymmetric
891   Hurricane Boundary Layer Structure from Dropsonde Composites in Relation to the
892   Environmental Vertical Wind Shear. *Monthly Weather Review*, *141*(11), 3968-
893   3984. https://doi.org/10.1175/MWR-D-12-00335.1
894
895   Zhang, F., & Emanuel, K. (2016). On the Role of Surface Fluxes and WISHE in Tropical Cyclone
896   Intensification. *Journal of the Atmospheric Sciences*, *73*(5), 2011-
897   2019. https://doi.org/10.1175/JAS-D-16-0011